

# RETRIEVAL OF SURFACE REFLECTANCE FROM AERIAL IMAGERY BY CALIBRATION WITH SATELLITE DATA

Dugal Harris and Adriaan Van Niekerk

## Abstract

While VHR aerial imagery holds great potential for quantitative remote sensing, its use has been limited by unwanted radiometric variation over temporal and spatial extents. In this paper we propose a simple, yet effective technique for transforming the digital numbers of aerial images to surface reflectance values. A collocated and concurrent, well calibrated satellite image is used as a surface reflectance reference to which the images are calibrated. The reference satellite sensor needs to be spectrally similar to the aerial sensor. It is shown that a spatially varying local linear model can be used to approximate the relationship between the surface reflectance of the reference image and digital numbers of the aerial images. The model parameters are estimated, for each satellite pixel location, using least squares inside a small sliding window. The technique was applied to a set of 2228 overlapping aerial images captured with an Intergraph DMC camera. A near-concurrent MODIS MCD43A4 image was used as the reflectance reference dataset. The resulting DMC mosaic was compared to a near-concurrent SPOT 5 reflectance image of the same area, and the mean absolute reflectance difference was found to be 4.18%, which compares well to the accuracy of other aerial image correction methods. The technique implicitly corrects for atmospheric and coarse-scale bidirectional reflectance distribution function (BRDF) effects and does not require spectral measurements of field sites or placement of known reflectance targets and produces seamless mosaics. Due to its relative simplicity and computational efficiency, it is an attractive alternative to existing calibration methods.

**Index Terms:** Aerial images, calibration, surface reflectance, BRDF correction, atmospheric correction

## 1 Introduction

VHR aerial and drone imagery is increasingly being used in remote sensing studies. The high spatial resolution of these images enables analyses on a finer spatial scale than most satellite based platforms can provide and consequently allows the exploitation of information such as

Dugal Harris (\* corresponding author) is with the Department of Geography and Environmental Studies, Stellenbosch University, Stellenbosch 7602, South Africa (email: dugalh@gmail.com)  
Adriaan Van Niekerk is with the Center for Geographical Analysis, Stellenbosch University, Stellenbosch 7602, South Africa (email: avn@sun.ac.za)

texture, object-based features and unmixed pixel spectra that is not available in lower resolution images (Chandelier and Martinoty, 2009; Collings et al., 2011; Honkavaara et al., 2009; López et al., 2011; Markelin et al., 2012). Accurate geometric calibration techniques for producing orthorectified images are well established and form part of typical aerial imagery processing workflows (Chandelier and Martinoty, 2009). Because aerial image mosaics are commonly produced for the purpose of visual interpretation, techniques such as dodging and look up tables (LUTs) are often used to produce smooth and visually appealing results (López et al., 2011). This kind of adjustment can damage the spectral information content and is not suited to quantitative remote sensing. Ideally quantitative analyses should be carried out on reflectance values, but extraction of surface reflectance from aerial imagery remains a challenge. Also, spatial and temporal radiometric variations in aerial imagery limit the extent over which quantitative remote sensing techniques can be successfully applied (Markelin et al., 2012). Atmospheric influences, bidirectional reflectance distribution function (BRDF) effects and sensor variations all contribute to radiometric variations in the imagery. To obtain surface reflectance, these radiometric variations must be reduced as far as possible.

There is some confusion and ambiguity around the use of reflectance terminology in the literature (Schaeppman-Strub et al., 2006). In this paper “surface reflectance” is used to mean the bi-directional surface reflectance at local solar noon and viewed at nadir. It is worth noting that as it is not possible or practical to correct for all the sources of radiometric variation in aerial imagery and that surface reflectance in most so-called “corrected” or “calibrated” images is only an approximation to the actual value.

A number of techniques for the correction of BRDF effects are available, including the popular kernel-based method (Roujean et al., 1992). Approaches based on radiometric transfer modelling (RTM), such as ATCOR (Richter, 1997), MODTRAN (Berk et al., 1999) and 6S (Vermote et al., 1997) are used for atmospheric correction. While these atmospheric and BRDF correction methods are effective on single images (Markelin et al., 2012), blocks of multiple aerial images present new challenges. The large view angles of aerial imaging cameras cause the solar and viewing geometries to vary significantly through the image (Lelong et al., 2008). Aerial campaigns are usually carried out over multiple days resulting in

significant variation in BRDF and atmospheric conditions. Each land cover also has its own unique BRDF and corrections should ideally model each of these covers separately (Collings et al., 2011; Honkavaara et al., 2009). Techniques that account for land cover specific BRDF's require an upfront cover classification which is time-consuming and introduces another potential source of error. Aerial campaigns can also consist of thousands of images making it impractical to apply time consuming atmospheric and BRDF correction models to every image (López et al., 2011). Even if it was practical, remnant radiometric variation due to the inexact nature of BRDF and atmospheric corrections will result in discontinuities, or seam lines, between adjacent images.

Approaches to calibrating mosaics of aerial imagery are receiving increasing attention (Chandelier and Martinoty, 2009; Collings et al., 2011; Gehrke, 2010; López et al., 2011). All of these approaches exploit the fact that adjacent images contain significant portions of overlap and that in a perfectly calibrated mosaic, these overlapping portions of different images should be identical. Collings et al. (2011) introduced a spatially varying linear model to perform combined atmospheric and BRDF correction. The parameters of the model are solved by minimising a cost function that considers the internal accuracy of each image, similarity of overlapping image regions and smoothness (i.e. the lack of seam lines) of the mosaic. In a second stage the entire mosaic is calibrated to absolute reflectance using specially placed ground targets with known reflectance. In Chandelier & Martinoty (2009) a simple three parameter model of the combined atmospheric and BRDF effects is fitted by minimising the difference between "radiometric tie-points", which are a selection of points in the overlapping image regions. It is a relative calibration method and no adjustment to absolute reflectance is made. A similar approach is used in López et al. (2011). Gehrke (2010) uses standard atmospheric and BRDF methods followed by a relative radiometric normalisation (RRN) step using invariant points in overlapping regions to smooth the mosaic.

A disadvantage of the aerial mosaic calibration techniques described above is their complexity and need for known ground references to achieve transformation to absolute surface reflectance. Transformation to an absolute physical quantity such as reflectance is beneficial as this is an invariant property of the surface which allows the data to be used in physical models, fused with other reflectance data and used in multi-temporal studies

(Downey et al., 2010; Vicente-Serrano et al., 2008). The options of placing targets of known reflectance to be captured as part of the mosaic or measuring the reflectance of suitably invariant sites on the ground are often not possible or practical. Many applications make use of archived imagery that had been captured prior to the commencement of the research and for which concurrent ground measurements are consequently not possible. Another approach is to make use of vicarious calibration involving knowledge of the spectral characteristics of specific ground sites, but this is recognised as being labour-intensive and costly (Chander et al., 2004; Gao et al., 2013; Liu et al., 2004).

In this paper, we propose a method of estimating surface reflectance from aerial imagery by calibrating to a coarse-resolution, concurrent and collocated satellite image that has already been corrected for atmospheric and BRDF effects. Satellite programs such as MODIS, make such coarse-resolution surface reflectance products freely available. Unlike existing methods for correction of aerial images, the proposed method avoids the need to perform time consuming and complex atmospheric and BRDF corrections explicitly. It also avoids the need for placement of known reflectance targets or field spectral measurements which can be impractical and time-consuming in many instances. The technique was applied to a set of 2228 overlapping aerial images captured with an Intergraph DMC camera. A near-concurrent MODIS MCD43A4 image was used as the reflectance reference dataset. The resulting DMC mosaic was compared to a near-concurrent SPOT 5 reflectance image of the same area.

## 2 Methods

### 2.1 Formulation

Combined BRDF, atmospheric and sensor corrections can be modelled as a spatially varying linear relationship between surface reflectance and sensor measurement. Following the notation of López et al. (2011), the aerial sensor measurement for each band can be expressed as:

$$= \rho_0 + \rho_1 \quad (1)$$

where  $L_s$  is the sensor measurement,  $L_0$  is the radiance at the sensor and  $a_0$  and  $a_1$  are coefficients determined by the characteristics of the sensor. The radiance at the sensor is expressed as:

$$L_s = \frac{L_0}{1 - a_0 - a_1} \quad (2)$$

where  $R_s$  is the reflectance at the sensor,  $E_0$  is the top of atmosphere (TOA) irradiance and  $\theta$  is the solar zenith angle. The reflectance at the sensor is described by the radiative transfer equation (Vermote et al., 1997):

$$R_s = R_a + \frac{R_s \tau_a \tau_s}{1 - \tau_a \tau_s} \quad (3)$$

where  $R_a$  is the atmospheric reflectance,  $R_s$  is the surface reflectance and  $\tau_a$  is the atmospheric albedo.  $\tau_a^\uparrow$  and  $\tau_a^\downarrow$  are the atmospheric transmittances due to molecular and aerosol scattering between the surface and sensor and between the sun and the surface respectively and  $\tau_a$  is the global atmospheric transmittance due to molecular absorption. The atmospheric albedo,  $\tau_a$ , is typically around 0.07 (Manabe and Strickler, 1964). With a small value for  $\tau_a$ , the denominator in Equation (3) is approximately one and the reflectance at the sensor can be approximated as:

$$R_s \approx R_a + \tau_a \tau_s \quad (4)$$

Equations (1), (2) and (4) express the relationship between the sensor measurement, atmospheric conditions and the surface reflectance. Note that the surface reflectance in Equation (4) represents the simplified case of a Lambertian reflector (i.e. it reflects equally in all directions), but in practice is subject to BRDF effects and so also varies with the viewing geometry. With the approximation of Equation (4), there is a linear relationship between surface reflectance and the sensor measurement. The parameters of this relationship are dependent on the atmospheric conditions and viewing geometry, and vary spatially and temporally. This linear relationship can be expressed as:

$$L_s = a_0 + a_1 R_s \quad (5)$$

where

$$= \frac{1}{-0 \uparrow \downarrow} \quad (6)$$

and

$$= 1 + \frac{1}{-0} \quad (7)$$

The parameters and , are spatially varying functions of the viewing geometry and atmospheric conditions. Use of a local linear relation to model radiative transfer is also advocated in Collings et al. (2011) and Gehrke (2010). Implicit in any radiometric calibration technique is an approximation of these parameters so that the relationship can be inverted.

In our proposed method, we solve for and of the aerial sensor using a reference estimate for the surface reflectance parameter, , obtained from a well calibrated satellite image. The reference surface reflectance image should have been captured at a similar time to the uncalibrated aerial image(s) to avoid phenological or structural differences between the reference and uncalibrated images. The reference image will typically be at a substantially lower spatial resolution than the aerial imagery. Calibrated surface reflectance products, such as those produced from MODIS and MISR, have resolutions of the order of 500m while aerial images usually have resolutions of 2m or higher. This large resolution discrepancy is not ideal, but it is assumed that atmospheric and BRDF effects vary little at a small spatial scale and that the reference resolution is sufficient to capture gradual variations in atmospheric conditions and BRDF. Real BRDF can vary significantly over short distances where land cover is heterogeneous. We regard the assumption of slowly varying BRDF as a necessary limitation of the method, and it is one that is shared by others (Chandelier and Martinoty, 2009; Collings et al., 2011; Gehrke, 2010; López et al., 2011).

Least squares estimates of and , for the aerial sensor, are found for each pixel of the reference image inside a sliding window, as described by Equation (8).

$$[ ] = [ ]^{-1} \quad (8)$$

where  $\mathbf{r}$  and  $\mathbf{c}$  are row vectors of the  $N$  values inside the sliding window and  $\mathbf{1}$  is a row vector of ones of length  $N$ .  $\mathbf{r}$  is obtained from the reference image and from the aerial image(s). The sliding window should consist of at least two pixels to solve for the two parameters. In circumstances where the camera offset,  $\mathbf{1}$ , is zero and atmospheric reflectance,  $\mathbf{c}$ , is small,  $\mathbf{C}$  may be regarded as being sufficiently small to be omitted from the model, in which case a sliding window of one pixel may be used. In order to accommodate the differing spatial resolutions,  $\mathbf{r}$  must be found at the reference spatial resolution, resampled to the aerial spatial resolution, and then used to estimate surface reflectance at this resolution by inverting the relationship of Equation (5).

The procedure follows these steps:

1. Resample uncalibrated aerial images to the reference image resolution and grid.
2. Calculate estimates of  $\mathbf{r}$  and  $\mathbf{c}$  for each pixel of each band of the reference image using Equation (8). This forms two multi-band rasters  $\mathbf{M}$  and  $\mathbf{C}$ .
3. Resample  $\mathbf{M}$  and  $\mathbf{C}$  rasters to the aerial image resolution and grid.
4. Calculate estimated surface reflectance for each pixel of each band of the uncalibrated aerial image, using Equation (5).

It is important to note that the proposed method assumes the spectral responses of the reference and uncalibrated sensors are identical. In practice, this does not hold true. The relation between surface reflectance and sensor measurement in Equation (5) becomes non-linear when including the spectral response effect. The surface reflectance in Equation (5) is a band-averaged quantity as represented by Equation (9).

$$\bar{r} = \frac{\int r(\lambda) \rho(\lambda) d\lambda}{\int \rho(\lambda) d\lambda} \quad (9)$$

where  $r(\lambda)$  is the spectral surface reflectance and  $\rho(\lambda)$  is the sensor relative spectral response (RSR) for a particular band. Without knowledge of the surface reflectance spectra, it is not possible to completely calibrate for this effect. However, for real world surface reflectances it can often be shown that the relationship between the band averaged values for different sensors is approximately linear (Gao et al., 2013; Jiang and Li, 2009). This means the relationship between surface reflectance and sensor measurement remains approximately linear even when the sensor spectral response is considered. Although the calibration method

proposed in this paper does not explicitly compensate for sensor spectral responses, it is assumed that the effect is locally linear and will consequently be incorporated into the model of Equation (5). This assumption is supported with simulations for the case study sensors in Section 2.3.

The choice of resampling algorithms in steps 1 and 3 of the procedure are important, especially when there is a large difference in the spatial resolution of the aerial and reference images. Optical imaging systems are linear and thus subject to the superposition principle which manifests as spectral mixing (Akhmanov and Nikitin, 1997). Averaging the uncalibrated image over each reference pixel area is recommended when downsampling in step 1. This will approximate the spectral mixing that occurs in the larger reference image pixels, although it does not account for the sensors' differing point spread functions (PSFs).

In our approach it is assumed that the effect of differing PSFs is negligible.

Standard interpolation algorithms were tested for efficacy when upsampling in step 3. It is necessary to produce smooth  $\mathbf{M}$  and  $\mathbf{C}$  rasters in this step to satisfy the assumption of slowly varying atmospheric and BRDF effects and to avoid discontinuities in the final image(s). Cubic spline interpolation, with its constraints of continuity of the first and second derivatives, was found to best satisfy this requirement. The Geospatial Data Abstraction Library (GDAL) (GDAL Development Team, 2014) was used for implementing the resampling.

Blocks of aerial surface reflectance images generated with the procedure outlined above can be mosaicked without the need for additional colour balancing or normalisation procedures to reduce seam lines. Because a single wide swath width reference satellite image will typically cover many aerial images, the calibrated images tend to combine into a seamless mosaic. Consideration must however be given to treatment of boundary pixels in steps 1 and 3 to minimise the formation of seam lines in the mosaic. For instance, when downsampling to the reference resolution in step 1, boundary pixels in the downsampled image that are only partially covered by aerial resolution pixels should be discarded as they can skew the estimates of  $M$  and  $C$ , especially for heterogeneous land covers. The condition of complete coverage can be relaxed somewhat to reduce discarded pixels. A condition of at least 90



percent coverage was used for our case study. When upsampling to the aerial resolution in step 3, the GDAL spline interpolator extrapolates pixels that lie outside the polygon formed by the centres of the reference resolution boundary pixels. This can cause discontinuities between adjacent images where extrapolation is inaccurate. Boundary conditions can be imposed on the spline interpolation to guarantee continuity between adjacent images, but if there is sufficient overlap between adjacent images, a simpler option is to discard the extrapolated boundary pixels before forming the mosaic. This is the approach that was adopted for the case study.

## 2.2 Study Site, Data Collection and Preparation

The surface reflectance retrieval method proposed in this paper was tested in a 96km x 107km area (Figure 1Error! Reference source not found.) in the Little Karoo in South Africa. Very high resolution (VHR) 0.5m/pixel multi-spectral aerial imagery was acquired from the Chief Directorate: National Geo-spatial Information (NGI), a component of the South African Department of Rural Development and Land Reform. The imagery was captured with a multispectral Intergraph DMC camera with red, green, blue and near-infrared (NIR) channels.

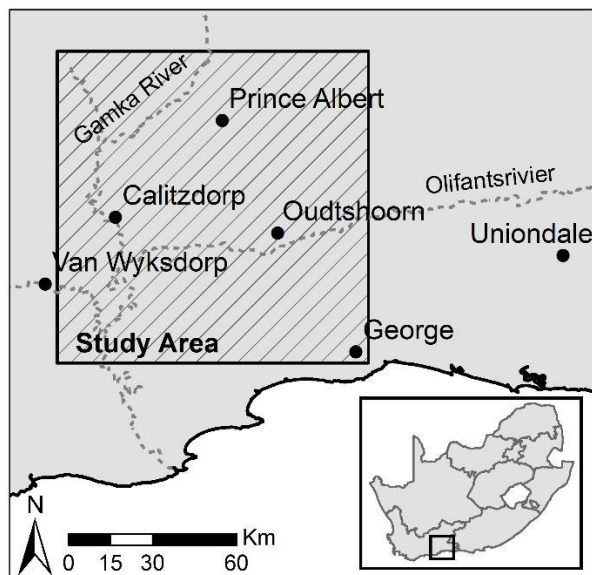


Figure 1 Study area orientation map

The RSR's of the DMC and MODIS sensors are shown in Figure 2. The peak overlap between the sensors is good in all bands with the exception of NIR.

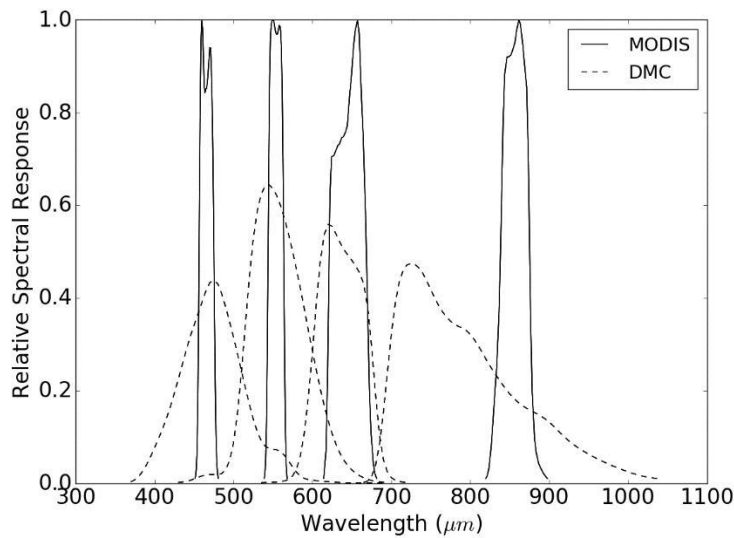


Figure 2 DMC and MODIS RSR's

The study site is covered by 2228 images captured during four separate aerial campaigns flown over multiple days from 22 January 2010 to 8 February 2010. The site was selected as the calibration work forms part of a larger vegetation mapping study being done in the area. The raw NGI imagery was obtained and corrected for camera effects using the Intergraph Z/I Post-Processing Software (PPS). The PPS corrected imagery was orthorectified using existing aero-triangulation data supplied by NGI and a 5m resolution digital elevation model (DEM) (Van Niekerk, 2014).

A MODIS MCD43A4 composite image for the period from 25 January 2010 to 9 February 2010 was selected as a reference for the cross calibration. This image has a 500m resolution and contains nadir BRDF-adjusted reflectance (NBAR) data composited from the best values over a 16 day period. The MODIS NBAR data has been processed with atmospheric and BRDF correction procedures (Strahler et al., 1999) and is recognised as a reliable reference source for cross calibration (Gao et al., 2013; Jiang and Li, 2009; Li et al., 2012; Liu et al., 2004). The NBAR data accuracy has been verified in a number of studies (MODIS Land Team, 2014). It was also selected as it has similar spectral bands to the Intergraph DMC. Bands 4, 1, 3 and 2 from the MODIS sensor were used to correspond to the red, green, blue and NIR bands from the DMC sensor respectively. The PPS processed imagery has zero

offset, so the parameter 1 from Equation (7) was zero and the atmospheric reflectance,  $\rho_a$ , was small as the surveys were flown on clear days. Thus,  $C$  was assumed to be small enough to be ignored and only the gain,  $M$ , was estimated. With only one parameter to estimate, a sliding window of one pixel was used to achieve the best possible spatial resolution in the  $\mathbf{M}$  raster.

### 2.3 Accuracy Assessment

In formulating the method in Section 2.1, it was assumed that effect of sensor RSR on measured surface reflectance is locally linear and can be incorporated in the model of Equation (5). To investigate the validity of this assumption, MODIS and DMC band averaged values were simulated for typical surface reflectance spectra and statistically compared. Twenty surface reflectance spectra were selected from the “soil”, “vegetation”, “water” and “man-made” classes in the ASTER spectral library (Baldrige et al., 2009) to represent commonly encountered land covers. Band averaged values were then calculated using Equation (9), with the MODIS and DMC RSR’s as shown in Figure 2.

Given that the DMC imagery was acquired in 2010, it was not possible to assess the accuracy of the reflectance retrieval method using ground-based spectral measures. Alternative methods for evaluating the results were consequently used. Firstly, the DMC DN and calibrated surface reflectance images were stitched into mosaics and the mosaics were visually compared to determine if discontinuities between adjacent images were reduced and to what extent the radiometric variations were corrected. Secondly, the DMC surface reflectance mosaic was resampled to the MODIS grid and resolution and statistically compared to the MODIS reference image. Lastly, we quantitatively compared the DMC surface reflectance mosaic to a SPOT 5 scene. The 10m resolution SPOT 5 level 1A image, acquired on 21 January 2010, covers portions of all four aerial campaigns as shown in Figure 3. The image was ortho-rectified using a 5m resolution digital elevation model (Van Niekerk, 2014). The SPOT 5 DN image was converted to surface reflectance using the Atmospheric/Topographic CORrection (ATCOR-3) method (Richter, 1997). Since the SPOT 5 sensor does not have a blue band, it was omitted from this validation. The DMC surface reflectance mosaic was resampled to the SPOT 5 resolution and grid, and statistically compared to the SPOT 5 surface reflectance image using Equation (10).

$$(\cdot) = |(\cdot) - (\cdot)| \quad (10)$$

where is the DMC mosaic, is the SPOT 5 image,  $(\cdot)$  are the pixel co-ordinates and is the difference image. The difference image was used to identify spatial patterns in the discrepancies between the corrected SPOT 5 image and DMC mosaic.

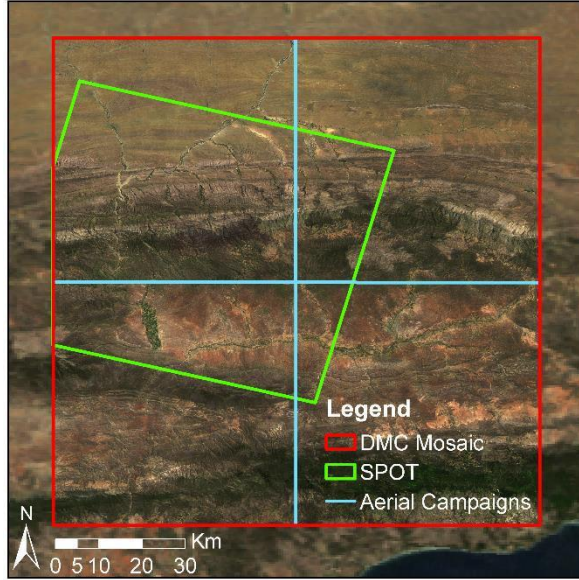


Figure 3 SPOT 5 scene and mosaic extents

### 3 Results and Discussion

#### 3.1 Band Averaged Relationships

The measured band-averaged reflectance relationship, for typical surface reflectances, between the two sensors is shown in Figure 4 with  $r^2$  values. The correlation between the DMC and MODIS band-averaged values (Figure 4) is surprisingly strong and supports the incorporation of the band averaging effect into the linear reflectance model of Equation (5). Similar linear relationships between different sensors for real world surface reflectances are reported in Gao et al. (2013) and Jiang and Li (2009). As the proposed method only requires the relationship to be locally linear, the variety of land covers simulated here is unlikely to be present inside the sliding window used to estimate the model parameters. For a small sliding window the correlation of the band averaged values will consequently be stronger than what is shown in Figure 4.

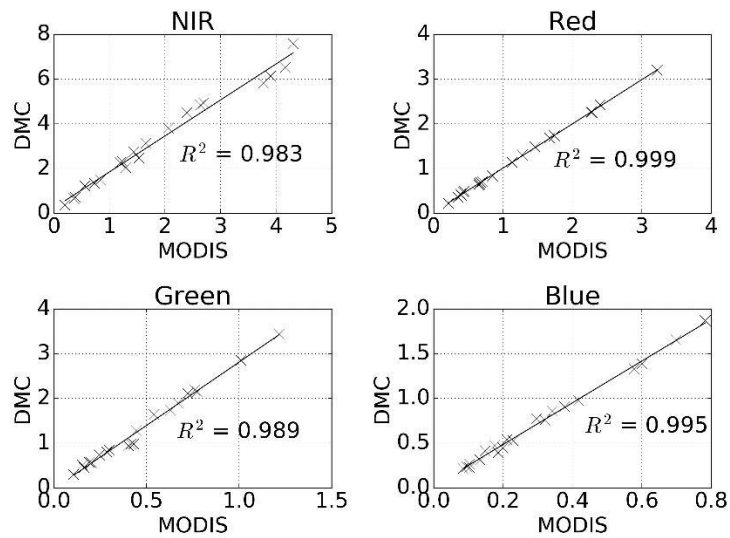


Figure 4 DMC vs. MODIS band averaged relationship for typical surface reflectances

### 3.2 Mosaicking

Figure 5 shows a RGB mosaic of DMC DN images (bordered in red), against a background of the MODIS reference image. Seam lines between adjacent DMC images and radiometric variations over the set of images are clearly visible.

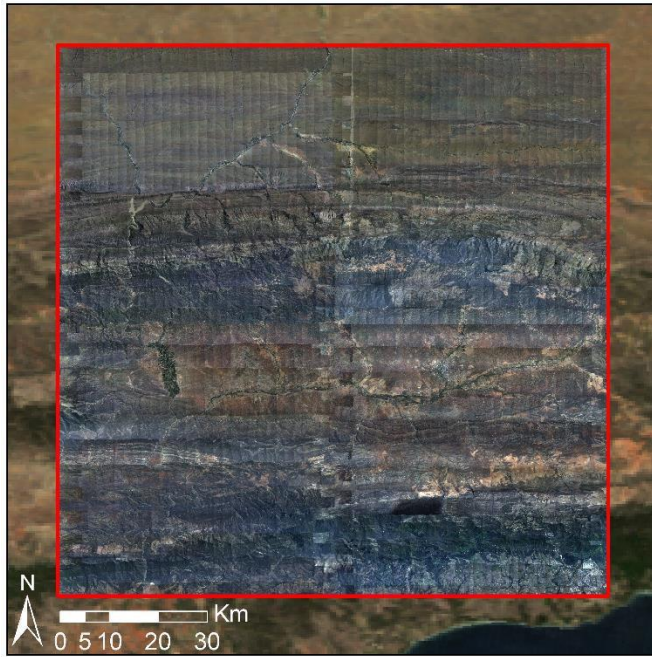


Figure 5 Uncalibrated mosaic on MODIS reference image background

Each DMC image was converted to surface reflectance using the proposed procedure. A RGB mosaic of the corrected images is shown in Figure 6, bordered in red, against a background of the MODIS reference image. No seam lines or radiometric issues (e.g. hot spots) are apparent at this scale, and the corrected images match the reflectance of the MODIS reference image.





Figure 6 Radiometrically calibrated mosaic on MODIS reference image background

Figure 7a shows a close-up section of the DMC DN mosaic where a hot spot (i.e. a BRDF effect where sunlight is strongly reflected back into the camera) and seam lines between adjacent images are visible. Figure 7b demonstrates the successful removal of the hot spot and seam lines after correction with the surface reflectance extraction method.

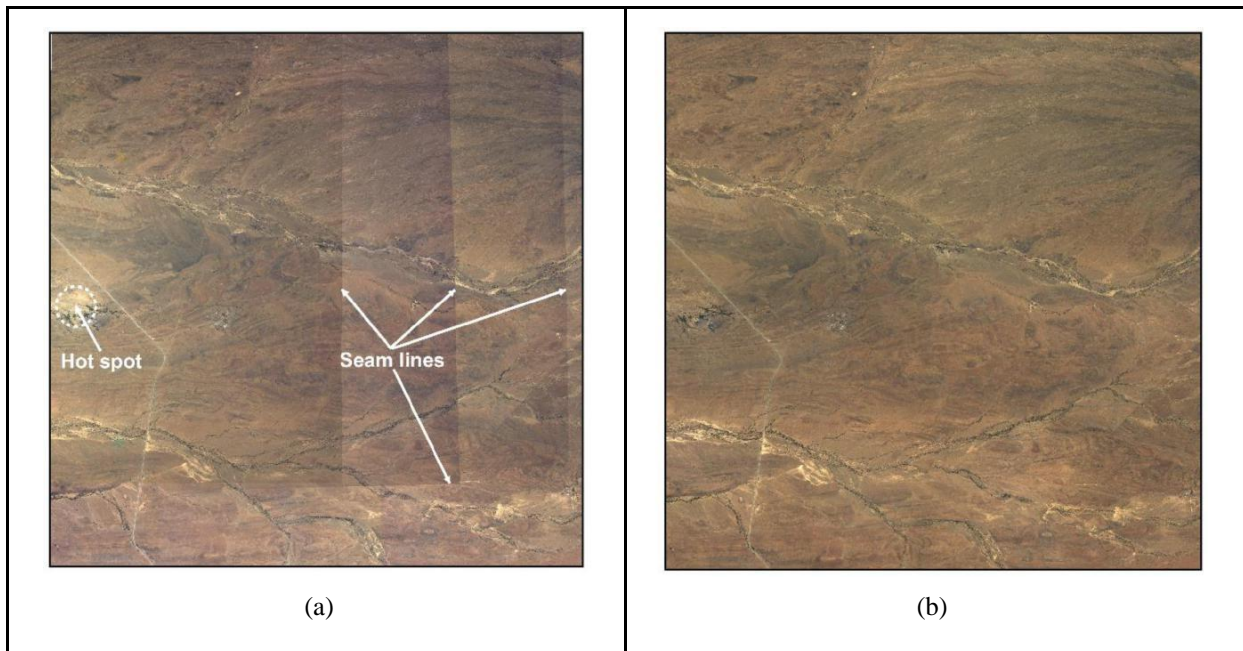


Figure 7 Reduction of hot spot and seam lines, with (a) showing raw DN images including hot spot and seam lines and (b) the corrected surface reflectance image

### 3.3 MODIS Comparison

Figure 8 shows scatter plots of the DMC DN and MODIS surface reflectance values with  $R^2$  coefficients indicating correlation strength. Figure 9 shows similar scatter plots for the DMC and MODIS surface reflectance values. Differences in the MODIS and DMC surface reflectance values at MODIS resolution are due in part to the use of the cubic spline interpolation to upsample the **M** and **C** rasters from the MODIS to DMC resolution. The spline interpolation is non-invertible (i.e. downsampling the upsampled rasters does not produce the original **M** and **C** rasters but successively smooths the data at each application). As indicated by Figure 8 and Figure 9, the correlation of the DMC and MODIS values is significantly improved when using the extracted DMC surface reflectance rather than DN values. This improvement in correlation is not unexpected, as Figure 9 is effectively comparing calibrated values to the values that were used for calibration. Nevertheless, this comparison serves as a general check on the validity of the method and as an indication of the effect of spline interpolation between the disparate MODIS and DMC resolutions. Mean absolute difference (MAD), root mean square (RMS), standard deviation and coefficient of determination statistics are given for the DMC and MODIS surface reflectance values in Table 1. Reflectance differences are greatest in the NIR band most likely due to the dissimilar MODIS and DMC RSRs in this band (Figure 2). This demonstrates the importance of using a reference image from a sensor with similar RSRs to those of the target imagery.

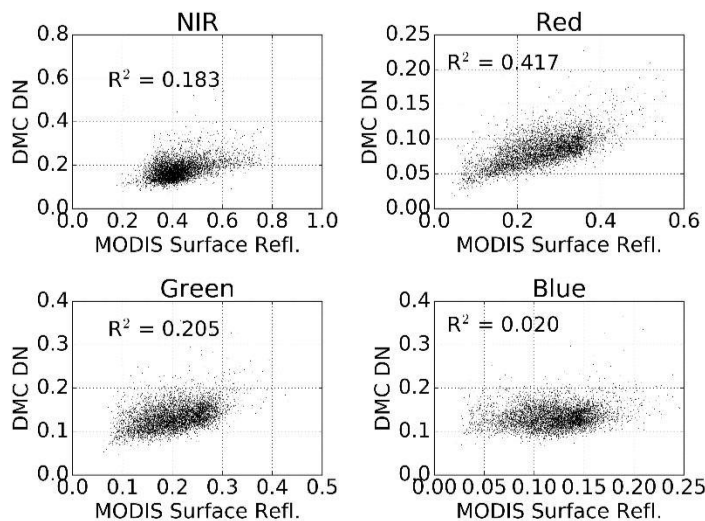


Figure 8 DMC DN mosaic and MODIS surface reflectance correlation



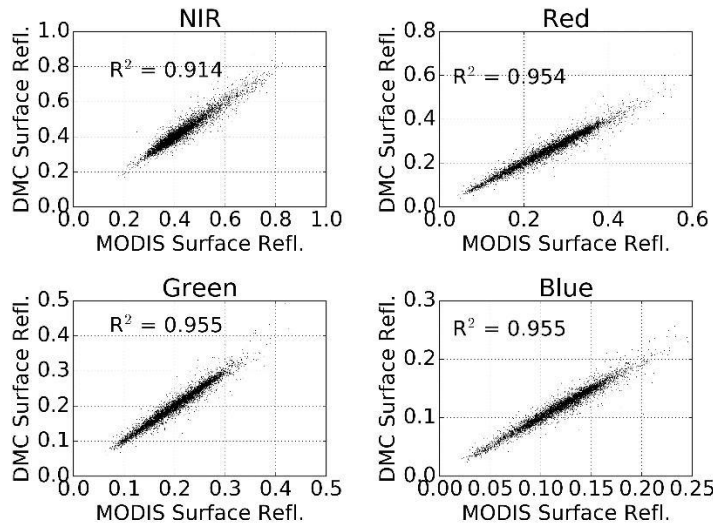


Figure 9 DMC surface reflectance mosaic and MODIS surface reflectance correlation

Table 1 Statistical comparison between MODIS and DMC surface reflectance images

Band(s)	Mean Abs. Diff. (%)	Root Mean Square (%)	Std. Dev. Diff. (%)	$R^2$
Near infrared	1.70	2.50	2.50	0.91
Red	1.18	1.75	1.75	0.95
Green	0.79	1.16	1.16	0.96
Blue	0.48	0.69	0.69	0.96
<b>All</b>	<b>1.04</b>	<b>1.67</b>	<b>1.67</b>	

### 3.4 SPOT 5 Comparison

The SPOT 5 resolution of 10m allows the surface reflectance result to be checked at a resolution significantly closer to the aerial resolution than the reference MODIS resolution. This provides a useful check of the assumption that BRDF and atmospheric variations occur gradually and can thus be approximated at the coarse scale of the reference image. While the MODIS comparison is checking the DMC surface reflectance against the reference it was fitted to, the SPOT 5 comparison is using an independent and “unseen” source.

Statistics for the reflectance difference between the corrected SPOT 5 image and the DMC surface reflectance mosaic are shown in Table 2. Not all of the reflectance differences can be

attributed to errors in the calibrated DMC surface reflectances. Spatial misalignment of pixels due to ortho-rectification differences and errors in the SPOT 5 surface reflectance also contribute to the recorded differences. The relatively low mean overall absolute reflectance difference of 4.18% is consequently a good indication that the surface reflectance extraction method is effective. These reflectance differences compare well to figures reported by other aerial image correction methods. Collings et al. (2011) achieved RMS reflectance errors of 4-10% measured on placed targets of known reflectance for their aerial mosaic correction technique, and in the aerotriangulation approach of López et al. (2011), mean absolute reflectance differences of 3-5% were obtained on field measured test sites, distributed throughout their study area. Similarly to the MODIS comparison, the largest reflectance differences occur in the NIR band. Again, this is likely due to dissimilarities in the MODIS, DMC and SPOT 5 sensor NIR RSR's (see Figure 2 and Figure 11). Scatter plots of DMC DN and SPOT 5 surface reflectance values are shown in Figure 12 and DMC surface reflectance and SPOT 5 surface reflectance values are shown in Figure 13 with  $R^2$  coefficients indicating correlation strength. The conversion to DMC surface reflectance provides a substantial improvement in correlation between the DMC and SPOT 5 values.

False colour CIR (colour-infrared) renderings of the DMC, SPOT 5 and difference images are shown in Figure 10. The contrast stretched difference image shows that most discrepancies occur in the rugged mountainous areas that extend west to east in the northern section of the scene and in densely vegetated areas along river banks in the southern section of the scene. Disparities in the mountainous areas are mainly due to differing shadow effects which are likely caused by variations in the time of day when the images were captured (the aerial photographs were captured throughout the day, while the SPOT 5 image was captured at 8:29am). A particularly bright area is noticeable in the upper right corner of the difference image. This corresponds to an area of bare ground which is bright in both the DMC and MODIS images and likely corresponds to a BRDF correction failure. It is not possible to say if this failure is in the SPOT 5 and or DMC corrections. The differences in the densely vegetated and cultivated areas are attributed to the differences in the MODIS, DMC and SPOT 5 sensor NIR RSR's being amplified by the known high NIR reflectivity of vegetation. Abrupt changes in BRDF may occur between adjacent fields in cultivated areas along the major rivers. These changes may not be captured at the MODIS resolution and could also be contributing to the NIR differences in these regions.

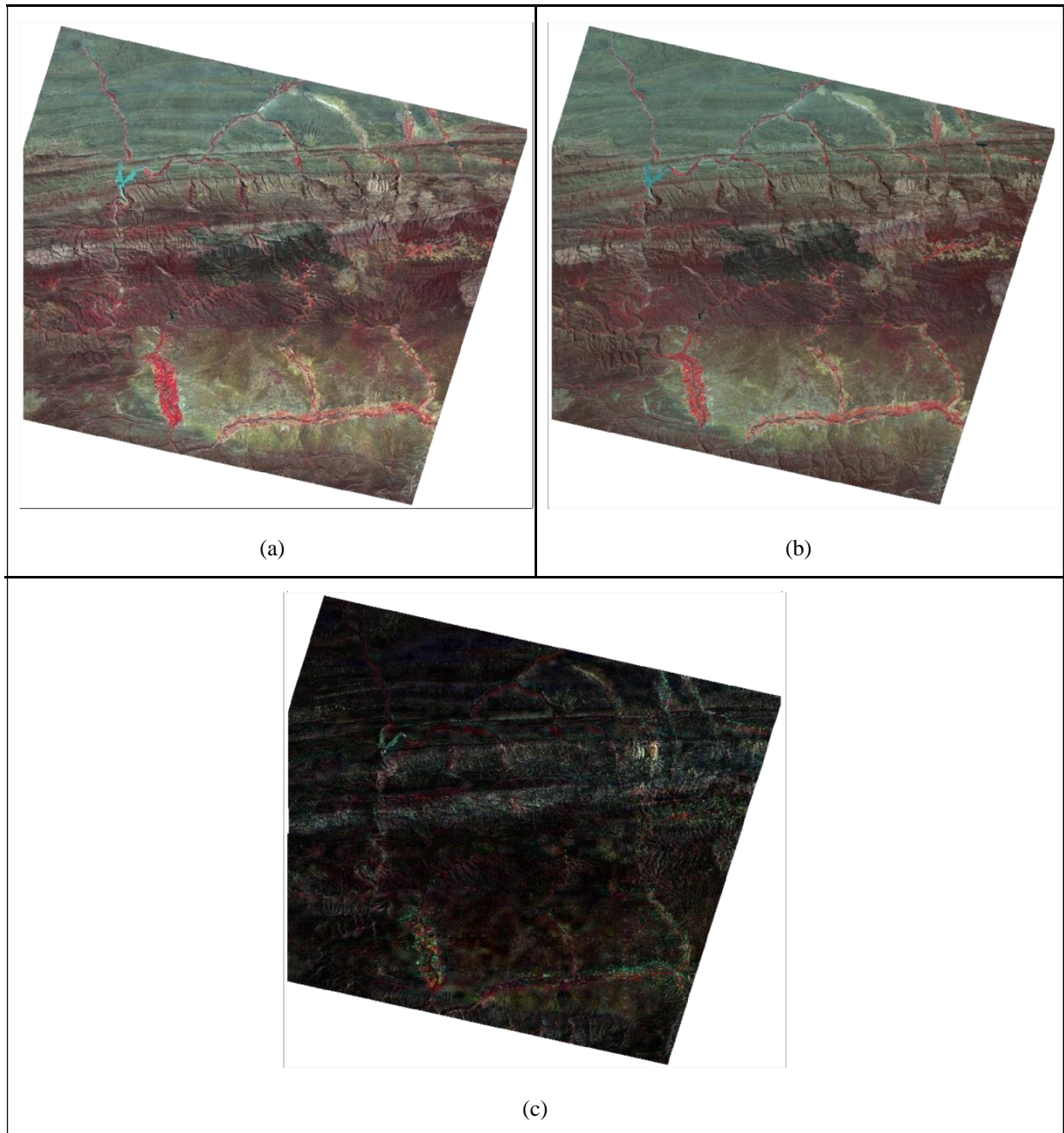


Figure 10 DMC and SPOT 5 surface reflectance comparison with (a) DMC surface reflectance mosaic masked to SPOT 5 extent; (b) SPOT 5 surface reflectance image; and (c) contrast stretched absolute difference image.

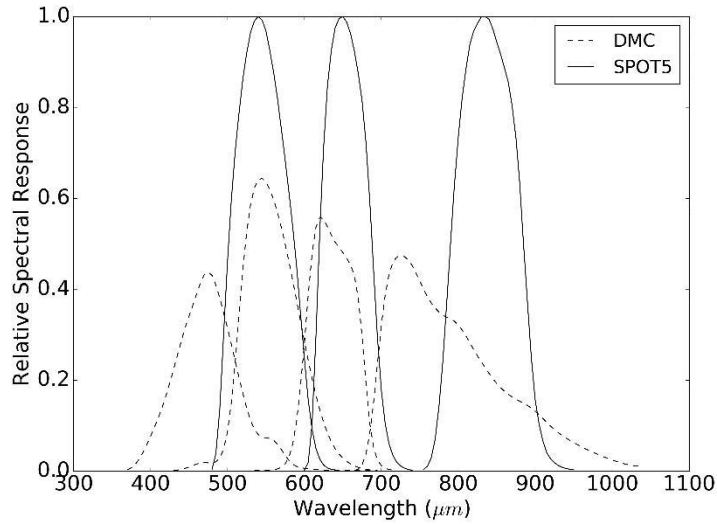


Figure 11 DMC and SPOT 5 RSR's

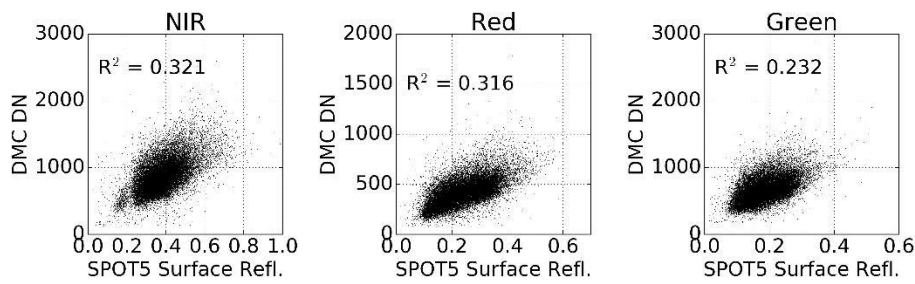


Figure 12 DMC DN mosaic and SPOT 5 surface reflectance correlation

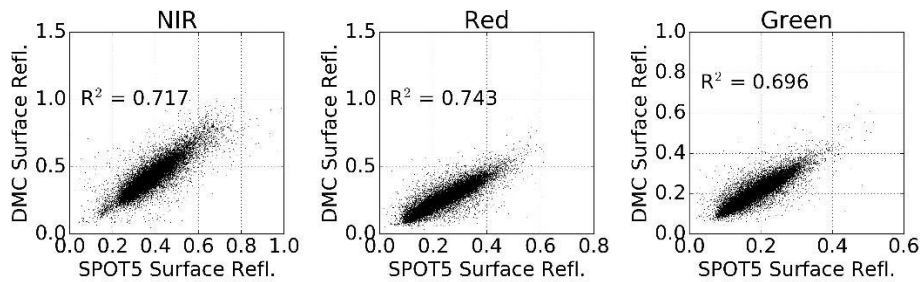


Figure 13 DMC surface reflectance mosaic and SPOT 5 surface reflectance correlation

Table 2 Statistical comparison between SPOT 5 and DMC surface reflectance images

Band(s)	Mean Abs. Diff. (%)	Root Mean Square (%)	Std. Dev. Diff. (%)	$R^2$
Near infrared	5.88	7.72	6.18	0.717
Red	3.74	5.42	4.84	0.743
Green	2.93	4.29	3.65	0.696
All	4.18	5.99	5.11	

## 4 Conclusions

This study proposes a method of estimating surface reflectance from aerial imagery by calibrating to a coarse-resolution, concurrent and collocated satellite image that has already been corrected for atmospheric and BRDF effects. The model parameters are estimated, for each satellite pixel location, using least squares inside a small sliding window. The proposed surface reflectance extraction method was applied to 2228 Intergraph DMC images covering an area 96 x 107km in size. A MODIS MCD43A4 image was used as the surface reflectance reference. The extracted DMC surface reflectance mosaic was free of visible seam lines and hot spots and matched the MODIS reference well. The DMC surface reflectance mosaic was also compared to a concurrent SPOT 5 image in order to establish the method efficacy at a spatial resolution closer to that of the DMC source resolution than the MODIS reference. The SPOT 5 image was corrected for atmospheric effects and converted to surface reflectance using the ATCOR-3 method. The mean absolute reflectance difference between the DMC mosaic and SPOT 5 image was 4.18%. This reflectance difference is considered supportive of the method's accuracy and is similar to figures reported by Collings et al. (2011) and López et al. (2011) for more complex correction techniques.

The proposed technique is simpler and computationally more efficient than existing aerial image correction approaches as it avoids the need for explicit BRDF and atmospheric correction as well as mosaic normalisation techniques to reduce seam lines. The spatially varying linear model allows for great flexibility in the BRDF characteristics that can be corrected for. It does however assume that BRDF and atmospheric variations are gradual and can be captured by the coarser resolution of the reference image. The extracted surface reflectance can also only be as accurate as the reference of course. According to the MODIS

land team (2014), the NBAR data used in the case study is accurate to “well less than 5% albedo at the majority of the validation sites”. The method is also limited by the need for a reference image concurrent and spectrally similar to the aerial imagery. Such an image may not always be obtainable. The MODIS and DMC RSR’s are quite different, particularly in the near infrared region of the spectrum (see Figure 2). The surface reflectance extraction method assumes the effect of different sensor spectral responses is linear and will be contained by the model of Equation (5). This assumption was confirmed by a simulation of MODIS and DMC measurements for typical land cover spectra. The relatively higher (5.88%) NIR reflectance difference between the DMC mosaic and the SPOT 5 values, and discrepancies in vegetated areas, are likely due to the more exaggerated differences in NIR RSR’s between the MODIS, DMC and SPOT sensors.

While the results of the surface reflectance extraction technique were surprisingly good given the simplicity of the method, some aspects warrant further investigation. Evaluation of the efficacy of using different sensors to provide the reflectance reference is of interest. Local terrain effects are poorly represented at the MODIS resolution. It would be informative to test the method with a higher spatial resolution reference such as Landsat Operational Land Imager (OLI). The MISR instrument is also a promising alternative to MODIS and could also be evaluated as a reflectance reference. MISR RSR’s are a better match to those of the Intergraph DMC than the MODIS bands, and it is possible to obtain 275m reflectance products using MISR-HR (Verstraete et al., 2012). Strong emphasis is placed on accurate calibration of the MISR data as its instrument captures data at nine different angles which allows a more accurate modelling of the BRDF compared to the kernel based approach followed in the calibration of the MODIS data (Strahler et al., 1999).

## **Acknowledgement**

We would like to thank Jan Vlok for proposing the vegetation mapping study that led to this research and for assistance in selecting the study area, Adrian Roos and Intergraph South Africa for providing a license for Intergraph PPS, Bernard Jacobs of Geospace International for assistance in understanding the NGI image processing workflow and in obtaining DMC RSR data, Theo Pauw and Garth Stephenson of CGA for assistance with computing and software resources and Julie Verhulp and NGI for provision of the aerial imagery. Lastly, we are grateful for funding from the Gamtoos Irrigation Board (GIB). GIB was otherwise not involved in this research.

## References

- Akhmanov, S.A., Nikitin, S.Y., 1997. *Physical Optics*. Clarendon Press, Oxford.
- Baldrige, A.M., Hook, S.J., Grove, C.I., Rivera, G., 2009. The ASTER spectral library version 2.0. *Remote Sensing of Environment* 113, 711–715. doi:10.1016/j.rse.2008.11.007
- Berk, A., Anderson, G.P., Bernstein, L.S., Acharya, P.K., Dothe, H., Matthew, M.W., Adler-Golden, S.M., Chetwynd, J.H., Richtsmeier, S.C., Pukall, B., Allred, C.L., Jeong, L.S., Hoke, M.L., 1999. MODTRAN4 radiative transfer modeling for atmospheric correction, in: *Proceedings of SPIE - The International Society for Optical Engineering*. Society of Photo-Optical Instrumentation Engineers, Denver, CO, pp. 348–353.
- Chandelier, L., Martinoty, G., 2009. A radiometric aerial triangulation for the equalization of digital aerial images and orthoimages. *Photogrammetric Engineering & Remote Sensing* 75, 193–200.
- Chander, G., Meyer, D.J., Helder, D.L., 2004. Cross calibration of the Landsat-7 ETM+ and EO-1 ALI sensor. *IEEE Transactions on Geoscience and Remote Sensing* 42, 2821–2831. doi:10.1109/TGRS.2004.836387
- Collings, S., Caccetta, P., Campbell, N., Wu, X., 2011. Empirical models for radiometric calibration of digital aerial frame mosaics. *IEEE Transactions on Geoscience and Remote Sensing* 49, 2573–2588. doi:10.1109/TGRS.2011.2108301
- Downey, M., Uebbing, R., Gehrke, S., Beisl, U., 2010. Radiometric processing of ADS imagery: using atmospheric and BRDF corrections in production, in: *ASPRS 2010 Annual Conference*. San Diego, CA, USA.
- Gao, C., Jiang, X., Li, X., Li, X., 2013. The cross-calibration of CBERS-02B/CCD visible-near infrared channels with Terra/MODIS channels. *International Journal of Remote Sensing* 34, 3688–3698. doi:10.1080/01431161.2012.716531
- GDAL Development Team, 2014. *Geospatial Data Abstraction Library* [WWW Document]. Open Source Geospatial Foundation. URL <http://www.gdal.org/>
- Gehrke, S., 2010. Radiometric processing of ADS imagery: mosaicking of large image blocks, in: *Opportunities for Emerging Geospatial Technologies*, American Society for Photogrammetry and Remote Sensing Annual Conference 2010 Held 26-30 April 2010. American Society for Photogrammetry and Remote Sensing, San Diego, USA, pp. 184–195.
- Honkavaara, E., Arbiol, R., Markelin, L., Martinez, L., Cramer, M., Bovet, S., Chandelier, L., Ilves, R., Klonus, S., Marshal, P., Schläpfer, D., Tabor, M., Thom, C., Veje, N., 2009. Digital airborne photogrammetry—A new tool for quantitative remote sensing?—A state-of-the-art review on radiometric aspects of digital photogrammetric images. *Remote Sensing* 1, 577–605. doi:10.3390/rs1030577
- Jiang, G.M., Li, Z.L., 2009. Cross-calibration of MSG1-SEVIRI infrared channels with Terra-MODIS channels. *International Journal of Remote Sensing* 30, 753–769. doi:10.1080/01431160802392638
- Lelong, C.C.D., Burger, P., Jubelin, G., Roux, B., Labbé, S., Baret, F., 2008. Assessment of unmanned aerial vehicles imagery for quantitative monitoring of wheat crop in small plots. *Sensors* 8, 3557–3585. doi:10.3390/s8053557
- Li, L., Yang, J., Wang, Y., 2012. Cross-calibration of HJ-1B/CCD1 image based on Aqua/MODIS data, in: *2012 Second International Workshop on Earth Observation and Remote Sensing Applications*. IEEE, Shanghai, China, pp. 116–119. doi:10.1109/EORSA.2012.6261147



- 981  
982  
983  
984 Liu, J.-J., Li, Z., Qiao, Y.-L., Liu, Y.-J., Zhang, Y.-X., 2004. A new method for cross-  
985 calibration of two satellite sensors. *International Journal of Remote Sensing* 25, 5267–  
986 5281. doi:10.1080/01431160412331269779
- 987 López, D.H., García, B.F., Piqueras, J.G., Guillermo, V.A., 2011. An approach to the  
988 radiometric aerotriangulation of photogrammetric images. *ISPRS Journal of*  
989 *Photogrammetry and Remote Sensing* 66, 883–893. doi:10.1016/j.isprsjprs.2011.09.011
- 990 Manabe, S., Strickler, R.F., 1964. Thermal equilibrium of the atmosphere with a convective  
991 adjustment. *Journal of the Atmospheric Sciences* 21, 361–385. doi:10.1175
- 992 Markelin, L., Honkavaara, E., Schläpfer, D., Bovet, S., Korpela, I., 2012. Assessment of  
993 radiometric correction methods for ADS40 imagery. *Photogrammetrie - Fernerkundung*  
994 *- Geoinformation* 2012, 251–266. doi:10.1127/1432-8364/2012/0115
- 995 MODIS Land Team, 2014. EOS validation status for MODIS BRDF/albedo: MCD43  
996 [WWW Document]. URL <http://tinyurl.com/jyx8gjs> (accessed 6.6.14).
- 997 Richter, R., 1997. Correction of atmospheric and topographic effects for high spatial  
998 resolution satellite imagery. *International Journal of Remote Sensing* 18, 1099–1111.
- 999 Roujean, J.-L., Leroy, M., Deschamps, P.-Y., 1992. A bidirectional reflectance model of  
1000 the Earth's surface for the correction of remote sensing data. *Journal of Geophysical*  
1001 *Research* 97, 20455. doi:10.1029/92JD01411
- 1002 Schaepman-Strub, G., Schaepman, M.E., Painter, T.H., Dangel, S., Martonchik, J.V., 2006.  
1003 Reflectance quantities in optical remote sensing—definitions and case studies. *Remote*  
1004 *Sensing of Environment* 103, 27–42. doi:10.1016/j.rse.2006.03.002
- 1005 Strahler, A.H., Wanner, W., Lucht, W., Schaaf, C.B., Tsang, T., Gao, F., Li, X., Muller,  
1006 J.P., Lewis, P., Barnsley, M.J., 1999. MODIS BRDF/albedo product: algorithm  
1007 theoretical basis document version 5.0 [WWW Document]. URL  
1008 <http://tinyurl.com/33zbxmn> (accessed 5.27.14).
- 1009 van Niekerk, A., 2014. Stellenbosch University Digital Elevation Model (SUDEM).  
1010 ResearchGate 16. doi:10.13140/2.1.3015.5922
- 1011 Vermote, E.F., Tanre, D., Deuze, J.L., Herman, M., Morcette, J.-J., 1997. Second  
1012 simulation of the satellite signal in the solar spectrum, 6S: an overview. *IEEE*  
1013 *Transactions on Geoscience and Remote Sensing* 35, 675–686. doi:10.1109/36.581987
- 1014 Verstraete, M.M., Hunt, L.A., Scholes, R.J., Clerici, M., Pinty, B., Nelson, D.L., 2012.  
1015 Generating 275-m resolution land surface products from the multi-angle imaging  
1016 spectroradiometer data. *IEEE Transactions on Geoscience and Remote Sensing* 50,  
1017 3980–3990. doi:10.1109/TGRS.2012.2189575
- 1018 Vicente-Serrano, S., Pérez-Cabello, F., Lasanta, T., 2008. Assessment of radiometric  
1019 correction techniques in analyzing vegetation variability and change using time series  
1020 of Landsat images. *Remote Sensing of Environment* 112, 3916–3934.  
1021 doi:10.1016/j.rse.2008.06.011